In situ analysis of residues resulting from laboratory impacts into aluminum 1100 foil: Implications for Stardust crater analyses

P. J. WOZNIAKIEWICZ[1, 2*], A. T. KEARSLEY[1], M. J. BURCHELL[3], N. J. FOSTER[3], M. J. COLE[3],
P. A. BLAND[2], and S. S. RUSSELL[1]

[1]Impacts & Astromaterials Research Centre (IARC), Department of Mineralogy, Natural History Museum (NHM), London SW7 5BD, UK
[2]IARC, Dept. Earth Science and Engineering, Imperial College London, South Kensington Campus, London SW11 2AZ, UK
[3]Centre for Astrophysics and Planetary Science, School of Physical Sciences, University of Kent, Canterbury, Kent CT2 7NH, UK
*Current address: Institute Geophysics and Planetary Physics, Lawrence Livermore National Laboratory, 7000 East Avenue,
Livermore, California 94550, USA
*Corresponding author. E-mail: wozniakiewic1@llnl.gov

Abstract–The encounter between the Stardust spacecraft and particles from comet 81P/Wild 2 gave impacts at a relative velocity of 6.1 km s^{-1} and near perpendicular incidence to the collector surface. Such conditions are well within the performance limits of light gas gun laboratory simulations. For this study, two series of shots were conducted at the University of Kent, firing magnesium silicates (Mg end-member forsterite, enstatite, diopside and lizardite), followed by a suite of increasingly Fe-rich olivines (through to Fe end-member fayalite) into Stardust flight-spare foils. Preserved residues were analysed using scanning electron microscopy combined with energy dispersive X-ray analyses (SEM/EDX). X-ray count integrals show that mineral compositions remain distinct from one another after impact, although they do show increased scatter. However, there is a small but systematic increase in Mg relative to Si for all residues when compared to projectile compositions. While some changes in Mg:Si may be due to complex analytical geometries in craters, there appears to be some preferential loss of Si. In practice, EDX analyses in craters on Stardust Al 1100 foil inevitably include contributions from Fe- and Si-rich alloy inclusions, leading to further scattering of element ratios. Such inclusions have complicated Mg:Fe data interpretation. Compositional heterogeneity in the synthetic olivine projectiles also introduces data spread. Nevertheless, even with the preceding caveats, we find that the main groups of mafic silicates can be easily and reliably distinguished in EDX analyses performed in rapid surveys of foil craters, enabling access to a valuable additional collection of cometary materials.

INTRODUCTION

The Al 1100 foils on the Stardust spacecraft (Brownlee et al. 2003) had the primary function of securing aerogel blocks in place and allowing safe removal upon return. However, they also provided an additional capture surface totalling 153 cm^2 (Tsou et al. 2003), upon which cometary materials may be examined in the form of impact residues in impact craters (Fig. 1). The return of the Stardust cargo after rendezvous with comet 81P/Wild 2, and the ensuing examination by the Preliminary Examination (PE) team, revealed the capture of many particles in both aerogel and foil (Brownlee et al. 2006; Hörz et al. 2006; Burchell et al. 2008a). The success of mineral interpretation for terminal particles extracted from aerogel (e.g., Zolensky et al. 2006), shows that

larger grains pose no great problems. However, the admixture of aerogel and remnants of finer particles along aerogel tracks (Zolensky et al. 2006; Trigo-Rodríguez et al. 2008) suggests that it may be useful to determine the composition of smaller grains within the aluminium foil craters where the impactor material may be retained in a limited area, and not dispersed over a large volume as is the case in some Stardust aerogel tracks where the impactor has broken up during capture. In addition, particles collected by aerogel cannot be readily analyzed in situ, generally requiring extraction and preparation for examination. With foils, the impact residues are thin, but located on the surface and are therefore exposed for immediate analysis. Fully exploiting this unique opportunity requires that we understand the impact process that occurs on foils. In particular, we need to determine
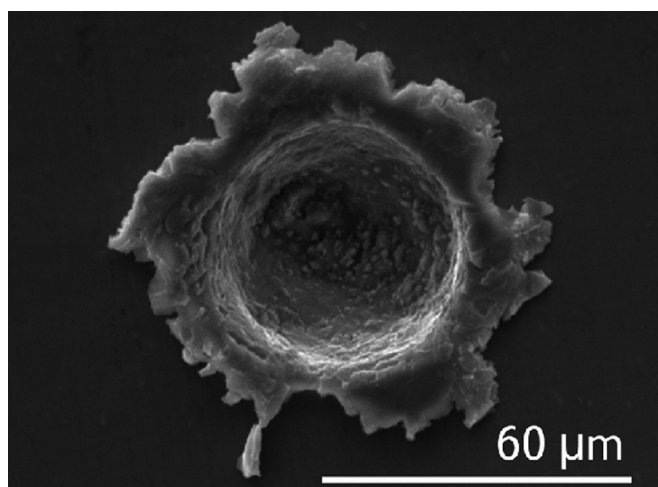
Fig. 1. Secondary electron (SE) image of Stardust crater C2009N,1. Impacting particles are preserved in the form of residues which line and roughen the crater surface.

whether it is possible to distinguish the most important minerals expected from cometary materials and to establish whether their compositions have been modified during capture.

The encounter conditions between Stardust and particles from comet 81P/Wild 2 (impact of 10s µm-sized particles, occurring at a relative velocity of 6.1 km s^{-1}, with incidence perpendicular to the collector surface [Brownlee et al. 2003]) can be replicated in the laboratory using light gas gun (LGG) techniques. In this paper, we discuss data from well characterized cometary analogue materials which have been shot at Stardust foils under appropriate conditions for comparison of the composition of the resulting residue with that of the original projectile.

For our initial study, conducted prior to the return of Stardust, a range of anhydrous magnesium silicates (Mg-rich olivine (Fo$_{89}$), enstatite and diopside) were chosen as representative of minerals likely to be contained within comets (Campins and Swindle 1998; Hanner 2003). In their summary of PE mineralogy and petrology studies, Zolensky et al. (2006) have now reported the common occurrence of these magnesium silicates, particularly olivines and (mostly low-Ca) pyroxenes, in Wild 2 dust. Amongst a wide range of other minerals, we have also fired powder of the hydrous magnesium silicate lizardite. The potential for recognition of phyllosilicates in crater residues has become particularly important in the light of infra-red spectra obtained for comet Temple 1 by the Spitzer Space Telescope, which have been interpreted as showing the presence of such minerals (Lisse et al. 2006). Micro-infrared spectroscopy taken from two Stardust aerogel particles have exhibited features that could possibly be attributed to hydrated minerals (Rotundi et al. 2008) although further investigation is required to confirm these findings. The occurrence of "bulbous"-shaped Stardust aerogel tracks, which have been generated when impacting

lizardite in laboratory experiments (Hörz et al. 2006; Burchell et al. 2008a), also indicate the possibility that hydrated minerals impacted the collector. To date however, no hydrated minerals have been positively identified in Stardust samples (Brownlee et al. 2006; Zolensky et al. 2008), although it would be unwise to state categorically from the limited number of samples analyzed so far that they will not be found elsewhere in the entire collector, or that they are necessarily rare in cometary bodies in general. We therefore believe that their recognition in crater residues will be important for future studies.

The four magnesium silicates noted above provided the initial silicate impact residues. The range of common compositions of olivines and pyroxenes found in Stardust and reported by Zolensky et al. (2006) prompted an extension of this work to incorporate a suite of olivines, ranging in composition from Mg-rich end-member forsterite, through to the Fe-rich end-member fayalite (Fo$_{100}$, Fo$_{80}$, Fo$_{60}$, Fo$_{40}$, Fo$_{20}$, and Fo$_0$). This paper presents the results from the first of our comparisons of composition before and after impact processing.

How Often Do Residues Remain?

An important question to answer before embarking on a program of work investigating the quality of residue on foils is: how often do residues remain within the crater? For the foils to play a major role in understanding the composition of comets, the preservation of residue must be a common occurrence. Over the past few decades much work on residues has been conducted on surfaces exposed in low Earth orbit (LEO), both as dedicated and non-dedicated residue collectors. These include Hubble Space Telescope (HST) solar arrays (Graham et al. 1997, 1999, 2001a; Kearsley et al. 2005, 2007a), multi-layer insulation foils, radiator and painted panels on the Space Flyer Unit (Yano et al. 1997, 2000), Al clamps on the Long Duration Exposure Facility (LDEF) (Bernhard et al. 1992, 1993, 1995), and a Ti alloy pressure tank from the Salyut 7-Kosmos 1686 spacecraft (Graham et al. 2001b).

Attempts to locate residues have met with mixed success. It was found that craters may preserve projectile materials in a variety of forms: solid fragments, solid fragments in a melt, and just melt. Of course some do not contain residue at all. This may partly reflect the conditions of capture. The velocities encountered in LEO vary widely: the projectile materials generally travel between 5 (lowest velocity particles are likely space debris) and 70 km s^{-1} (Graham et al. 2001b), with variation in these values due to geometry of the impacts (i.e., the direction of target motion and hence incidence angle relative to projectile motion). The velocity of impact directly affects the pressures reached, with higher velocities generating greater peak shock pressures and post-shock temperatures (e.g., Melosh 1989). These factors in turn affect

the level of modification undergone by the impacting materials, leading to ejection, melting and even vaporization of materials from the crater (Bernhard and Hörz 1995). The occurrence of some craters with no recognizable residue may reflect their formation by impact above a limiting velocity, beyond which no residue material is retained, or might reflect an impactor of such volatile composition as to leave no solid trace. The velocity of the Stardust encounter was relatively modest (6.1 km s^{-1}), and we might therefore expect a higher success rate in finding residues than seen on spacecraft in LEO. We must, however, remember that it is the compositional and structural properties of both the projectile and the target that determine the pressures reached during the impact event. The LEO investigations looked at diverse impact substrates, most being quite different in density and mechanical strength properties when compared to the Stardust collector foils. It is also quite difficult to make direct comparison between results from older and more modern analytical instruments, particularly as the availability of large computer memory resources now allows automated data collection, which is almost certainly more effective for the location of small discrete patches of impact residue in craters.

Laboratory experiments utilizing LGGs have also been numerous. After analyses of LDEF aluminium clamps had revealed the presence of craters both with, and without, preserved residue, the work of Bernard and Hörz (1995) aimed to investigate what encounter velocities were required to generate the "empty" craters. A series of experiments were performed, impacting soda-lime glass spheres (~3.2 mm in diameter) into Al 1100 sheets (2.5 to 4 cm in thickness) at velocities ranging from 1 to 7 km s^{-1}. The findings echoed those of the LEO surface analyses: velocities up to ~3 km s^{-1} resulted in the majority of projectile material preserved as solid fragmented blocks located in the crater, but with increasing amounts of melt above 2 km s^{-1}; above 3 km s^{-1} melt dominates. The amount of residue remaining begins to diminish after 4 km s^{-1}, assumed to be lost in vaporization processes. These results indicate that in Stardust foil impacts we should expect to see small amounts of residue, dominated by melted material. It must, however, be borne in mind that, while the velocity range used by Bernhard and Hörz covers that of the Stardust encounter, the properties of the materials were rather different to those on Stardust: the projectiles were much larger (3.2 mm spheres), and the aluminum foils were thicker (2.5 to 4 cm thick sheets). Perhaps a closer comparison to Stardust is given in the sub-mm particle impacts into 101 μm thick foil described in Kearsley et al. (2006, 2007b). These papers both find residue to be plentiful in craters generated by impacts under Stardust encounter conditions.

Another relevant observation is that of Burchell et al. (2008b) where impacts into aluminium 1100 at 6.1 km s^{-1} not only yield residues from a variety of minerals but also Raman signals are obtained from projectile fragments in the craters.

This was true for, amongst others, olivine and enstatite, although not for lizardite impactors. This suggests that in some impactors, on scales similar to those of the larger Stardust impacts, intact (and crystalline) projectile fragments have been retained in the foil craters. Indeed, Leroux et al. (2008) also report crystalline residues in Stardust foil craters.

To determine how often residues remain after impact in conditions directly comparable to those of Stardust, we examined the results of a shot of enstatite powder (Shot G270405#1 at 5.85 km s^{-1} into Al 1100). In total 72 craters between ~50 and ~100 μm in diameter (created by projectiles ranging from ~10 to 20 μm in diameter as determined from calibrations in Kearsley et al. 2007b) were examined using scanning electron microscopy (SEM) with energy dispersive X-ray microanalysis (EDX); 63 of these (89%) were found to contain recognizable magnesium silicate residue. Of the remaining 9 craters, 6 (8%) contained residue rich in Cu and Fe oxides, and 1 (1%) contained iron silicate. We believe these 7 craters to be impacts by particles originating within the gun itself, or rare contaminants in the projectile powders. From the final two craters, geometrical issues meant that residue lay beyond the scope of our detector preventing collection of spectra with confident elemental peaks; one crater was particularly deep; the other was a complete penetration (see the Imaging and Analysis Method section). It therefore appears that certainly the great majority of craters produced in this shot contained projectile residue. Indeed, preliminary results from Stardust craters also show this remarkable level of survival (Zolensky et al. 2006; Hörz et al. 2006; Flynn et al. 2006). We conclude that the survival of impact residue is unlikely to be the limiting factor in interpretation of Stardust Al foil craters.

Alteration During Impact

The majority of work regarding crater residues on spacecraft in LEO has focused on identifying whether the residue has an artificial (space debris) or natural (micrometeoroid) precursor. Stardust materials require more sophisticated classification, to identify specific minerals present in the impactor, and to compare results with those of grains captured in aerogel. Although there was a clear need to define mineralogy under Stardust encounter conditions prior to return of the Stardust payload, only recently have some authors attempted to identify the mineralogy of the projectile involved in cratering on Stardust (e.g., Kearsley et al. 2007a; Zolensky et al. 2006; Hörz et al. 2006). Such interpretation is thwarted by our poor understanding of what happens to the composition of mineral grains during impact. Does it remain the same? Is the precursor mineral even recognizable? To what types of minerals do such results apply? All or only a limited range? An earlier study of impacts on aluminum foil at 6 km s^{-1} (Kearsley et al. 2007b) had indicated that the residues of orthopyroxenes and olivines in separate shots

Table 1. A summary of the hypervelocity impact experiments described in this paper. All shots were performed on Stardust foil using the technique of Burchell et al. (1999).

Shot	Projectiles (NHM sample)	Projectile size and shape	Impact speed (km s^{-1}) $\pm$ 2%	Contaminants	Comments
G110505#1	Olivine (Fo$_{89}$) (BM 1950-337)	38–53 μm irregular	5.91	Minor Fe-sulfide	–
G270405#1 G110505#	Enstatite (BM.2005,M318)	<38 μm irregular	5.85 5.91	Minor Talc inclusions	–
G110505#1	Diopside (BM.2005,M310)	Polydispersive irregular	5.91	Minor inclusions of epidote and calcite	–
G130106#2	Lizardite (specimen awaiting cataloguing)	>500 μm irregular	5.91	Minor talc inclusions	Large grains fired, which break up during acceleration in the gun, giving smaller grain sizes at impact
G171106#3	Olivine Fo$_{100}$ (XRD laboratory standard)	>300 μm Porous irregular aggregates	6.08	Substantial silica, periclase and non-stoichiometric MgSi residual "melt"	
G171106#1 G14/02/07#2	Olivine Fo$_{80}$ (XRD laboratory standard)	>300 μm Porous irregular aggregates	6.01 6.21	Minor silica and substantial non-stoichiometric MgSi residual "melt"	
G171106#3	Olivine Fo$_{60}$ (XRD laboratory standard)	>300 μm Porous irregular aggregates	6.08	Substantial silica and non-stoichiometric MgFe oxide The olivine component itself varies in composition from Fo$_{59}$ to Fo$_{67}$	Small sample volume means cannot sieve Large grains fired, which break up during acceleration in the gun, giving smaller grain sizes at impact
G171106#1 G130207#1	Olivine Fo$_{40}$ (XRD laboratory standard)	>300 μm Porous irregular aggregates	6.01 5.99	–	
G041206#2	Olivine Fo$_{20}$ (XRD laboratory standard)	>300 μm Porous irregular aggregates	5.93	Minor iron oxide and silica	
G171106#3	Olivine Fo$_{0}$ (XRD laboratory standard)	>300 μm Porous irregular aggregates	6.08	Substantial iron oxide and silica	

were easily distinguishable on the basis of Mg to Si count ratios. In this current paper we assess the reliability of in situ mineral identification, and include a suite of olivine compositions to establish the extent to which original mafic silicate composition is preserved and determinable. For these new experiments, it was felt important to ensure that all the minerals had undergone the same level of impact processing, and they were therefore shot at very similar velocities.

SAMPLES AND METHODOLOGY

The LGG Shot Conditions and the Target and Projectile Materials

All laboratory impact experiments were performed using the LGG in the Centre for Astrophysics and Planetary Sciences at the University of Kent, Canterbury. The powder shot and velocity measurement techniques employed here are described in Burchell et al. (1999). In each shot the target chamber was evacuated to a few 10^{-1} mbar, or better, to minimize velocity loss in flight. The average impact speed

was 5.99 ± 0.11 km s^{-1} (see Table 1), measured individually in each shot with an accuracy to within 2%.

The target in each case was a sample of flight-spare Stardust Al 1100 foil (provided by P. Tsou of the Jet Propulsion Laboratory). This foil was ~101 μm thick (Kearsley et al. 2007a), and was wrapped around a square Al alloy plate (Al 6082) measuring ~1.5 cm × 1.5 cm, to simulate the mounting on the Stardust collector. This was then mounted upon an Al base-plate (10 cm × 10 cm), drilled with a hole in each corner both for support within the target chamber, and to enable handling throughout the shot and subsequent analysis without damage or contamination to the craters and their residues. Throughout this preparation procedure gloves and pliers were used to avoid contamination of the foil.

The projectiles used were all single phase—while most cometary particles appear to be polymineralic aggregates of small grains (Brownlee et al. 2006; Zolensky et al. 2006; Hörz et al. 2006), to understand how the residue may reflect complex particles, it is clearly a prerequisite that we understand the behavior of the main individual mineral

phases. The magnesium silicate projectiles originally chosen —olivine (Fo_{89}, specimen BM.1950,337), enstatite (specimen BM.2005,M318), diopside (specimen BM.2005,M310) and lizardite (specimen awaiting cataloguing)—were all taken from collections at the Natural History Museum (NHM), London. Finding homogeneous, natural samples of olivines with tightly clustered compositions, across the range of Fo-Fa, and of sufficient quantity for use as LGG projectiles, proved to be difficult. Instead we chose to use synthetic olivines (commissioned from Richard Brooker, Dept. of Earth Sciences, University of Bristol), employed as standards in the X-ray diffraction (XRD) laboratory of the NHM. The initial group of magnesium silicates were each crushed in a pestle and mortar to produce powders, before loading into the LGG sabot. The olivine suite, already provided in powder form, could not be crushed further due to small sample volume. Projectile size ranges were determined by imaging using the SEM (Table 1). The majority of these particles, if they were to reach the target intact, would generate craters at Stardust upper size limit or greater (particle-crater diameter correlation by Kearsley et al. 2007b). However, the acceleration experienced in the LGG is enough to cause the break-up of these particles, especially those of the weak lizardite and often aggregate synthetic olivines (as established by the SEM imaging), resulting in a whole array of crater diameters throughout the Stardust range.

The olivine, enstatite and diopside were all shot together in one sabot: shot G110505#1 at a velocity of 5.91 km s^{-1}. The lizardite was shot in a later firing: shot 13/1/06#2 at a velocity of 5.97 km s^{-1}. The suite of olivines were fired in several shots: Fo_{100}, Fo_{60} and Fo_{0} were fired together in shot G171106#3 at a velocity of 6.08 km s^{-1}: Fo_{20} was fired in shot G041206#2 at a velocity of 5.93 km s^{-1}: and Fo_{40} and Fo_{80} were fired twice, initially together in shot G171106#1 at a velocity of 6.01 km s^{-1}, and separately as shot G130207#1 (Fo_{40}) and G14/02/07#2 (Fo_{80}) at velocities of 5.99 km s^{-1} and 6.21 km s^{-1} (respectively). This re-firing was necessary because the first shot yielded very few impacts. While the velocities for each shot were slightly different, they were close enough for meaningful comparisons to be drawn. These shot details are compiled in Table 1.

Imaging and Analysis Instrumentation

A large array of analytical tools are available for residue analysis (e.g., Zolensky et al. 2000), which each present different advantages, but frequently with the disadvantage that they may cause varying degrees of damage to the sample. In order to maximize the return from the unique Stardust sample set, data must be obtained by non-destructive methods that require little sample preparation before moving on to more laborious and destructive techniques. Furthermore, as the number of Stardust craters is very large (Hörz et al. 2006), fast analyses by widely available techniques that permit the

recognition of interesting residue compositions as early in the investigation process as possible are vital. Scanning electron microscopy (SEM) and energy dispersive X-ray microanalysis (EDX) were our chosen methods of analysis, as they are largely non-destructive, relatively fast, widely available and allow data to be gathered from inside craters. All imaging and analysis for this investigation (including analyses of materials other than the primary foils) were conducted using the JEOL 5900 LV SEM in the Electron Microscopy and Mineral Analysis Division (EMMA) of the Department of Mineralogy at the NHM, London. An accelerating voltage of 20 kV, beam current of 2 nA and a working distance of 10 mm were used. Backscattered electron (BSE) images, secondary electron (SE) images and EDX microanalysis were done through an Oxford Instruments system, running version 16 INCA software. All spectral data were taken live and all foils were uncoated. Rough powder projectile samples of the initial magnesium silicates were also uncoated, however, the polished resin blocks of the olivine suite projectiles were carbon (C)-coated.

Imaging and Analysis Method

In order to determine whether the compositions of projectiles are preserved in their residues, SEM EDX analyses were required from both the raw projectile grains and the crater residues. The crater residue analysis setting can be described as a thin, usually insulating layer of impact residue (without a conductive carbon coating), lying within steep walled topographic depressions and overlying a rough surface of metal alloy. While the SEM is capable of quantitative EDX analyses, such a complex setting is so far from that conventionally used for quantitative microanalysis (i.e., polished, beam-perpendicular surfaces), that the standard correction routines available cannot be applied. Comparisons between the projectile and residue chemistries were therefore made based on their raw count data for the major element Kα lines.

For all analyzed foils, an automated electron-image montage mosaic was generated over the whole foil, to be used as a map for initial crater location. The next step was to determine the positions of ~5 craters over 50 μm in diameter generated by each of the minerals. From calibrations in Kearsley et al. (2007b) such craters are created by projectiles with diameters of ~10 μm and above. These craters are large compared to the majority of craters on the Stardust spacecraft, however, 63 Stardust craters >20 μm diameter have been identified so far, and it is the size range of particles responsible for these that make up the majority of the cometary dust mass which impacted the Stardust foil and aerogel (Kearsley et al. 2008). For those foils where only a single mineral was fired (Fo_{20} shot G041206#2, Fo_{40} shot G130207#1 and Fo_{80} shot G14/02/07#2) this was simply a matter of choosing random craters. For the lizardite-bearing
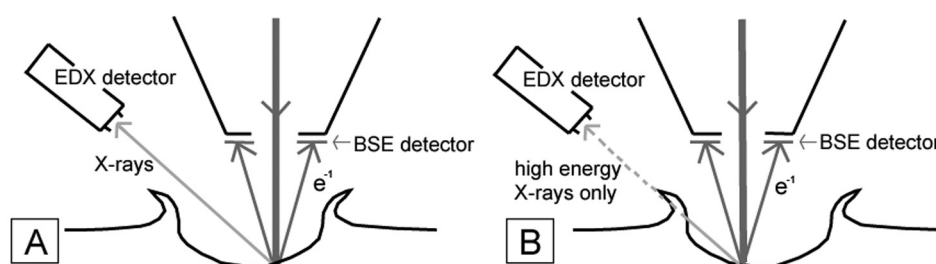
Fig. 2. The detection of X-rays by an inclined EDX detector over a rough (e.g., cratered) surface. In (A) the electron beam is incident on an area of the crater floor that is visible to the window of the EDX detector, and the detector receives all of the X-rays generated. In (B) the electron beam is incident on an area obscured from the EDX detector by the crater rim, therefore only a few high energy electron reach the detector.

foil of shot 13/1/06#2, where this was the only magnesium silicate in the projectile mix, locating lizardite craters required the generation of a set of X-ray maps for the entire foil, and cross referencing the various element maps to locate the Si and Mg signals. For the olivine, enstatite, and diopside-bearing foil of shot G110505#1, their chemical similarities would not be distinguishable in such a low resolution approach. Therefore an initial survey was required, involving several live 5-second point spectra being obtained from every crater over the entire foil. A similar survey was employed for the Fo_{100}, Fo_{60} and Fo_0 foil shot (G171106#3), and the Fo_{40} and Fo_{80} foil of shot (G171106#3).

Once the probable mineralogical source of all of the craters had been determined, ~5 craters were chosen for each mineral, and the locations of residue suitable for acquisition of X-ray data were found. Our first approach involved the collection of a series of 5-second spectra throughout the crater, but it was found that generating a short X-ray map over the crater was a less time consuming and more reliable method. Once an area of residue was located in a crater, a minimum of ten 50-second point spectra were taken.

The location of the EDX detector and the rough nature of the cratered surface required care as to where analyses were taken. While the BSE detector on the JEOL 5900LV is located at the base of the beam column (therefore receiving electrons from the total surface that interacts with the beam), the EDX detector is inclined at an angle of 40°. As a result, surface topography can cause shadowing as X-rays that are generated behind an obstacle to the detector line-of-sight, such as a crater wall, are blocked. In order to obtain a reliable spectrum it is necessary to avoid these shadow zones. We are therefore restricted to taking analyses from a narrow band around the crater lip and on the steep crater wall (Kearsley et al. 2007b). Unfortunately, this procedure is complicated further by the fact that the blocking of X-rays is energy dependent: that is to say, a larger (thicker) obstacle is required to block a high energy X-ray compared to a low energy X-ray (Fig. 2). Therefore, the extent of the shadowed region is also energy dependent, with higher energy X-rays having a smaller shadow region. As a result, when taking an analysis from just outside the shadow region of Fe ($K\alpha$ peak at ~6.4 keV) we

may still be in the shadow region of Mg ($K\alpha$ peak at ~1.2 keV) or even Si ($K\alpha$ peak at ~1.7 keV), and will therefore get spectra biased towards the higher energy Fe. In order to avoid such high energy biasing in our analyses, we must monitor the Bremsstrahlung region of the spectra. The Bremsstrahlung region is a background of X-rays with energies up to that of the beam, generated by inelastic interactions between the electrons of the beam and atoms of the sample, resulting in energy loss from the beam electrons. On a normal EDX detector in good working order, this background should have a plateau at ~2 keV where the efficiency of detection and number of X-rays generated together define a maximum (as described in Goldstein et al. 1992). When an area is in shadow, the preferential absorption of low energy X-rays will shift the plateau towards higher energies and the lower energy X-ray emission lines will appear to be superimposed on an upward sloping background. This is particularly noticeable in craters on Al foil, with a sharp drop in the background above the Al absorption edge at 1.5 keV, followed by an upward slope to the plateau, shifted to >2 keV (as shown in Kearsley et al. 2007a). Monitoring the position of the background peak allows us to discard those spectra affected by topographic shadowing phenomena.

Although all residue spectra were collected for the same dwell time, large variations in count numbers were found which we attribute to varied residue thickness. To ensure a spread in Mg and Si counts for the accompanying projectile analyses the spectrum collection times were varied (5, 10, 25, and 50 seconds). The resulting data were then presented in binary graphs of Mg against Si counts for the initial magnesium silicates, and in ternary graphs of Mg, Si, and Fe counts for the suite of olivines and initial magnesium silicates.

Potential Complications to Analyses

Impurities in the Projectiles

The initial magnesium silicate projectiles (olivine, enstatite, diopside and lizardite) were sourced from well characterized NHM specimens with negligible impurities. After preparation, a small amount of each projectile powder was examined using SEM EDX to confirm composition and

purity before use. BSE images were generated and accompanying X-ray maps were collected, colored and combined, to create compositional maps. From these it became clear that these projectile powders were no longer completely pure. The contaminants were single phase grains, with compositions matching previously prepared projectiles. During projectile preparation care was taken to clean the pestle, mortar and sieve between each mineral, however the size of the resultant grains meant that it was impossible to completely prevent transferral of a small portion of one powder to the next. There were also occasional silicate grains which exhibited lead signals in their spectra, indicative of an origin from the pestle and mortar itself. Using image analysis techniques available in the INCA software the area of the compositional maps occupied by the contaminant phases relative to the intended projectile was determined. We found that the powders comprised less than 5% contaminants in all cases. While this is low, it is necessary to be aware of the issue when analyzing the crater residues. We should recognize that a small percentage of residues may not fit with the expected spectra.

For the suite of olivines, analyses of polished grains from each composition, mounted in resin blocks, showed sample heterogeneity to be more of an issue. These samples were created in the laboratory, and as such it appears that they contain unassimilated pieces (up to 50 μm in size) of the precursor materials from which they were made (silica, periclase, iron oxide and an undetermined MgFe-rich phase) as well as intermediate melt components. Fo_{60} was the poorest quality projectile with the olivine varying in composition throughout the sample from Fo_{59} to Fo_{67}, and an MgFe-rich phase and silica making up roughly 25% of the material by area. Similar abundances of contaminating materials were found in the Fo_{100}, Fo_{80} and Fo_0, while less than 10% were found in Fo_{20}, and none was seen in Fo_{40}. With such large abundances of precursor materials and intermediate melt, a worrying possibility was that the olivine portions of these materials had not successfully crystallized, but were instead amorphous materials of olivine composition. However, work on this same suite of olivines using a variety of techniques (Mössbauer spectroscopy, X-ray diffraction, and Raman spectroscopy) has confirmed olivine crystallinity (Bland et al. 2004; Menzies et al. 2005; Foster et al. 2007). The contaminants within this suite of olivines will need to be borne in mind during interpretation of the results. A summary of the contaminants found in each projectile featured in this paper is given in Table 1.

Impurities in the Target

The standard composition of Al 1100 is greater than 99% Al by weight, with the majority of the remainder made up of Fe and Si (Davis 1998). Kearsley et al. (2006) found the Fe and Si content to be in the form of discrete Fe- and Si-rich inclusions that are spread randomly over the foil. They are
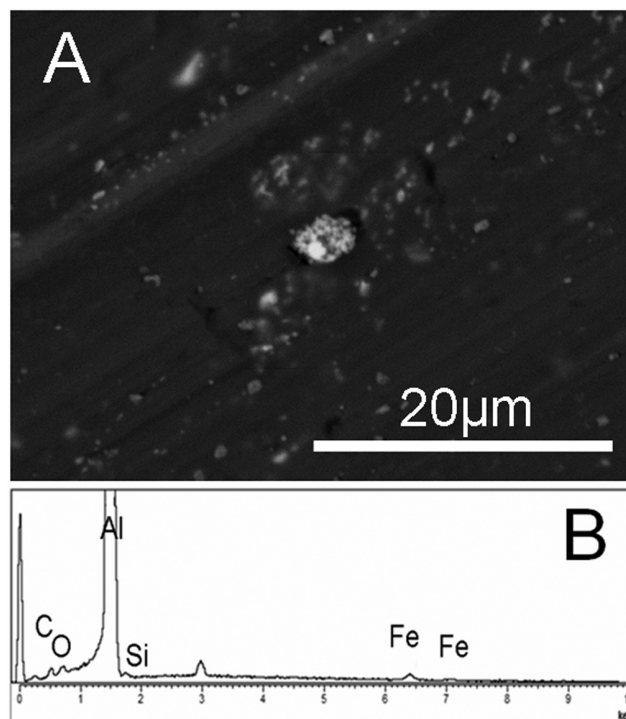

Fig. 3. Foil inclusions. A: BSE image of an area of clean, un-shot foil, displaying bright inclusions. B: Spectrum taken over the inclusion in the Stardust foil. The spectrum clearly displays the presence of Fe, O and minor Si and C superimposed upon the Al peak. The unnamed peak at 3 keV is an interference peak caused by the Al.

small, typically up to a maximum of a few μm in size, and therefore—although accounting for less than 1 weight% of the foil—they are numerous enough that the occurrence of an impact over such an inclusion may be commonplace. Indeed, a glance at the foil surface under SEM quickly reveals the presence of these inclusions (Fig. 3). If an impact occurs over the location of an inclusion we might well expect the inclusion to underlie or even mix with the residue and add to the spectra. Unfortunately, there is no way of determining if this is the case, and therefore the presence of these inclusions and their effect on our results must be borne in mind when interpreting our data.

Contamination from the LGG

With every shot of the LGG, a small portion of material is deposited throughout the gun barrel and chamber. This material may be part of the projectile, cartridge powder, sabot or material broken away from the inside of the gun itself. Shots therefore run the risk of contamination by such gun-derived debris (GDD). The extent of this contamination was evaluated by examining a foil used in a control (blank) shot in the LGG (i.e., the gun was fired as normal, but no projectiles were placed in the sabot). The surface of this foil was found to exhibit a fine coating of C and a littering of larger particles. These larger particles exhibit compositions that are Fe-, C- or
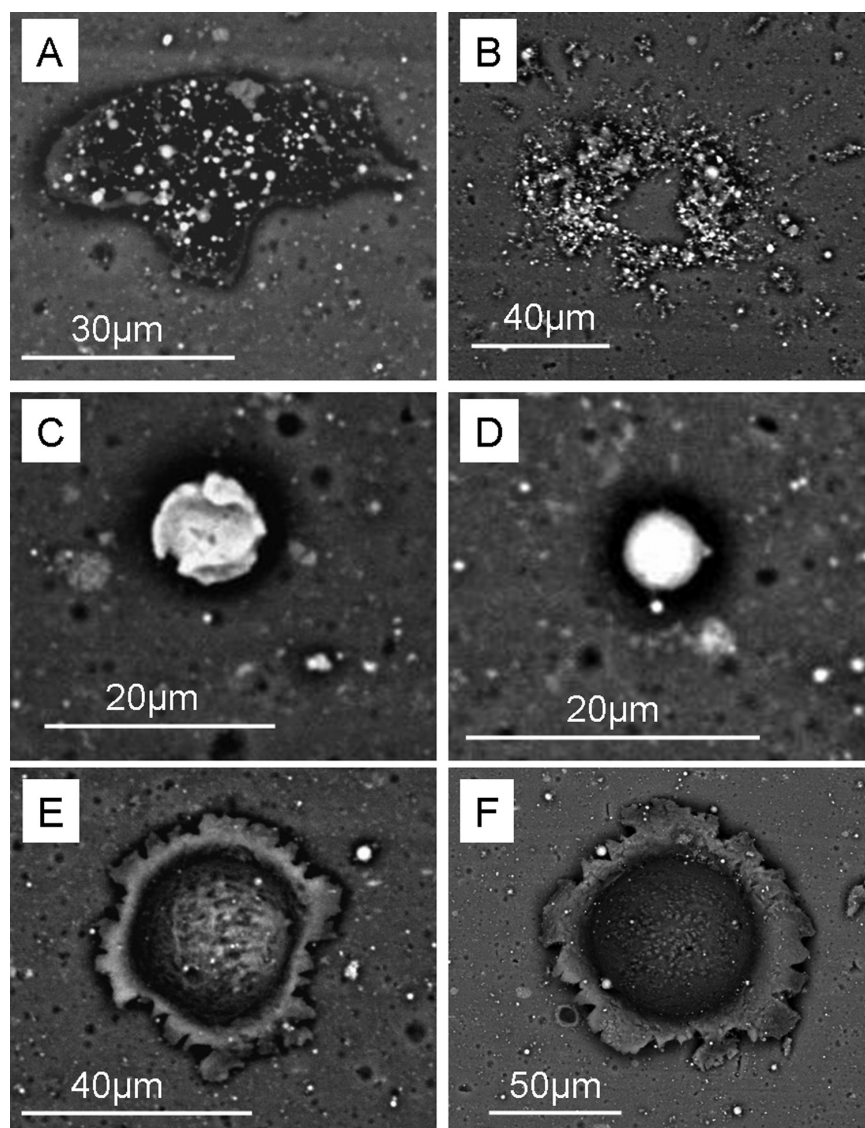
Fig. 4. Blank shot foil. A–D) BSE images of the most common types of large GDD seen on the blank-sabot shot target. These particles vary in shape from near spherical (C–D) to irregular (A–B), and in brightness and tend to be high in oxygen and carbon with a variety of silicon, iron and calcium levels. E: A crater created by GDD. F: A crater on the shot G110505#1 foil that both contains and is surrounded by GDD.

occasionally Si-rich oxides, often with accompanying minor concentrations of Ca, Mn, Cu, and Cl, and their morphologies range from perfect spheres to irregular composite structures (Fig. 4A–D). In some cases, these GDD materials have been accelerated to high enough velocities to enable them to produce craters on the surface of the foil (Fig. 4E).

The larger GDD are generally easy to spot and were avoided when taking analyses. The C-film covers the entire foil and is therefore unavoidable. While this does not affect our analyses of magnesium silicates, it does mean that such laboratory experiments cannot provide precise information on C-dominated minerals and organics. The craters that can be generated by GDD are similar in all aspects of morphology to those of our magnesium silicates (Fig. 4F), however, their residue compositions make their alternative origin clear.

When analyzing residues we remain aware of this and reject any analyses whose spectra do not contain the fundamental Mg, Si, and Fe peaks.

RESULTS AND DISCUSSION

Magnesium Silicates

For the initial suite of magnesium silicates, only Mg and Si counts were plotted in a simple binary diagram. The Mg to Si ratio was chosen as it provides an excellent but simple means by which to distinguish between these important cometary dust components. The results of this comparison are displayed in Figs. 5 and 6. Error bars of 1 standard deviation in the integrated peak (calculated by INCA software) were
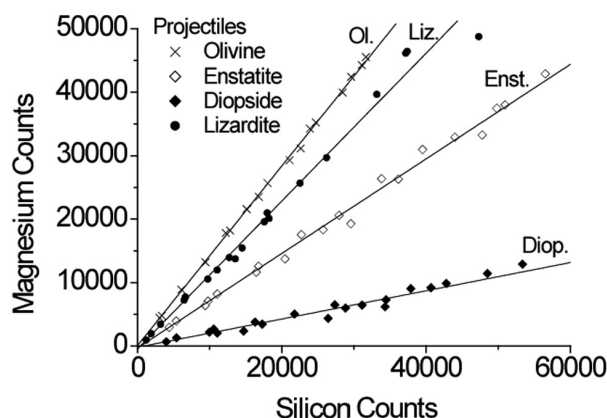
Fig. 5. Raw Mg and Si count integrals in EDX spectra taken from near horizontal areas on rough mineral powders of the initial magnesium silicate projectile materials. Solid lines represent the linear fits to these data (see Table 2 for fit curve values).
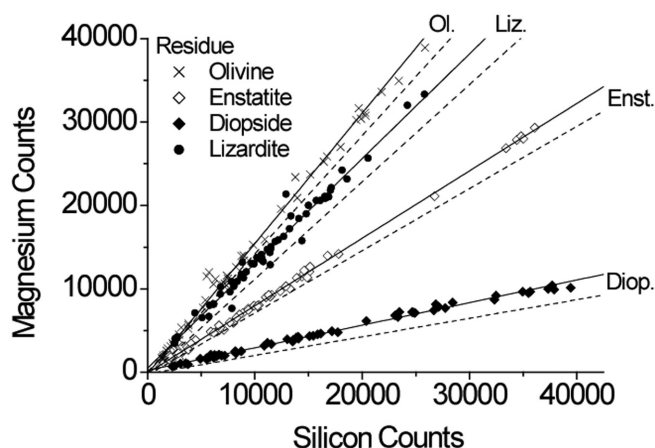

Fig. 6. Raw Mg and Si count integrals in EDX spectra taken from initial magnesium silicate impact residues on sloping crater walls. Solid lines represent the linear fit to these residue data, dashed lines represent a linear fit to the projectile data of Fig. 5 (see Table 2 for fit curve values).

originally plotted, however the error bars are all contained within the symbol for each data point so were not visible and have been removed.

The data for each of the magnesium silicates fit well defined linear trends. Results of linear fits (weighted by the 1σ errors) are given in Table 2, along with the goodness of fit criteria (the regression correlation coefficient r). The fit lines can be clearly separated from one another in both projectile and residue states, therefore we have a constant Mg to Si ratio for each mineral both before and after impact. There is, however, a positive shift in linear fit gradient from projectile to residue, suggesting an increase in Mg content relative to Si after impact. This shift in gradient between projectile and residue is different for the various minerals, with diopside displaying the largest change and lizardite the least (Table 2).

This increase in Mg relative to Si must be caused by either an actual change in the mineral composition during the impact process, or something inherent to the method of analysis of the residue and projectile. Next we discuss various options for the origin of this effect.

Angle of Beam-Sample Incidence

As has been discussed in the Imaging and Analysis Method section, the rough nature of the cratered surface results in shadows in the X-ray data, restricting the analyses to areas of residue residing on the small regions of the crater interior that remain "visible" to the detector. These areas are located on the steep interior walls of the crater, meaning that for residue analyses, the beam incidence was not perpendicular to the sample surface. As the projectile analyses were taken from horizontal surfaces (with perpendicular beam-sample incidence), the increase in Mg relative to Si for residues could simply be a result of such a difference in the analysis procedure.

To address this issue an experiment was devised whereby a petrographic thin section of the olivine (Fo_{89}) was tilted from horizontal to 80° in 10° increments and at each step five 50-second spectra were obtained. In tilting the sample there is an increased danger of colliding the sample into the BSE detector with any stage motions, therefore a working distance of 20 mm throughout was adopted (while not optimum for this detector, which normally operates with a separation of 10 mm, any effect of beam incidence angle would be apparent). The experiment ran over two days, therefore data for 30° tilt was collected on both days to allow correction to be made for any changes in beam conditions.

The effects of beam incidence angle on Mg, Si and Fe Kα X-ray counts are shown in Fig. 7. As the sample was tilted from horizontal to ~60°, the Mg and Si counts increased while those of Fe remained roughly constant. Beyond ~60° the counts of all three then fell. The Mg to Si ratio is plotted against tilt angle in Fig. 8 where it can be seen that as the sample is tilted from horizontal, the Mg initially increased relative to the Si, but this increase begins to level off at ~60°. An increase in Mg to Si ratio of ~7% is observed when tilting from 0° to 80°.

In order to understand the effect beam incidence is having on the Mg to Si count ratio, we consider a simple thought experiment. As the beam travels into the sample, it loses energy as its electrons undergo elastic backscattering, and the energy available for X-ray stimulation decreases resulting in lower energy X-rays produced with depth, until eventually no X-rays are generated (Fig. 9a). Consider a point "x" below the surface (Fig. 9b). As the sample is tilted from horizontal (Fig. 9c), two things happen:

1. The path length (the distance of sample that generated X-rays must travel through to be emitted to the detector) is decreased and therefore the magnitude of associated

Table 2. Summary of the fit curve equations and weighted correlation coefficient (r) values for projectile and residue EDX analyses of the initial magnesium silicates in Figs. 5 and 6.

| Mineral | Projectile (P) | | | Residue (R) | | | % Change in Mg/Si from P to R |
	Equation	r	Mg/Si	Equation	r	Mg/Si	
Olivine (Fo$_{89}$)	Mg = (46 ± 79) + (1.416 ± 0.006)Si	0.999	~1.42	Mg = −(177 ± 41) + (1.562 ± 0.005)Si	0.996	~1.56	~+10
Enstatite	Mg = −(325 ± 65) + (0.745 ± 0.003)Si	0.997	~0.74	Mg = (86 ± 45) + (0.808 ± 0.004)Si	0.999	~0.81	~+10
Diopside	Mg = −(199 ± 40) + (0.223 ± 0.002)Si	0.984	~0.22	Mg = (236 ± 38) + (0.271 ± 0.002)Si	0.997	~0.27	~+23
Lizardite	Mg = −(467 ± 55) + (1.165 ± 0.004)Si	0.996	~1.17	Mg = (506 ± 73) + (1.256 ± 0.007)Si	0.989	~1.26	~+8
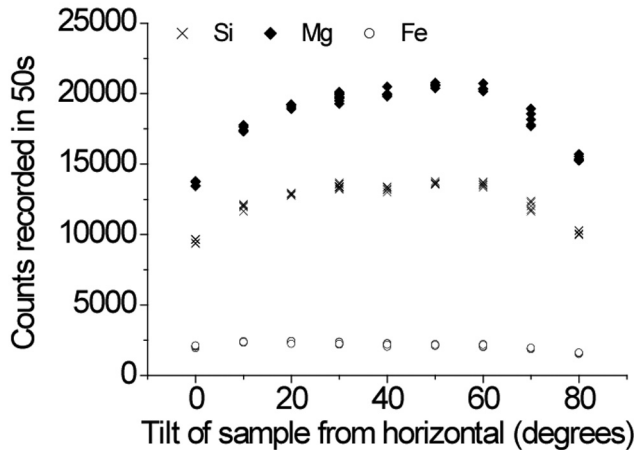
Fig. 7. Results of sample tilt experiment. 50-second spectra were taken from a polished thin section of olivine as it was tilted by 10° increments from 0° to 80°. Here Mg, Si and Fe count integrals are plotted against sample tilt angle. In most cases the readings from the 5 repeated measurements overlay each other.
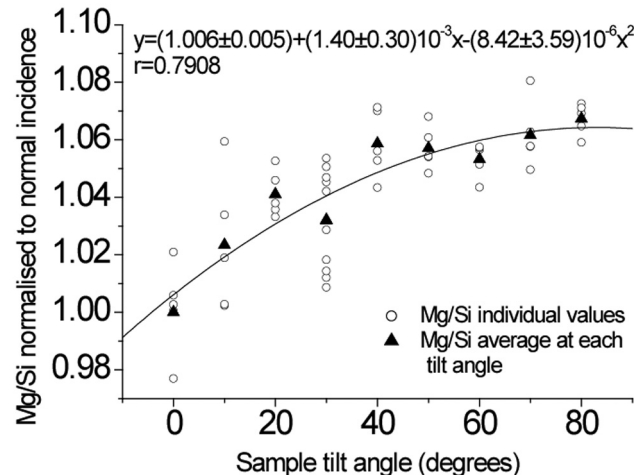

Fig. 8. Results of sample tilt experiment. 50-second spectra were taken from a polished thin section of olivine as it was tilted by 10° increments from 0° to 80°. Here the Mg to Si count integral ratio is normalized to the results for a horizontal sample and is plotted against the tilt of the sample. The trend line is fitted to the average Mg/Si values for each angle.

absorption is decreased. This means more of the generated X-rays should reach the surface. This is also known as the Absorption Effect (see description in Goldstein et al. 1992).

2. The X-ray generation volume decreases, meaning the number of X-rays generated decreases. This can be understood when we consider that as electrons interact with the sample and undergo elastic scattering, most scattering angles are so small that the electron tends to continue in the same general directions, after scattering—this is termed "forward scattering." With a 0° sample tilt the tendency for forward scattering causes most of the electrons to propagate down into the sample and generate X-rays. As the sample is tilted, more electrons propagate closer to the surface and can escape, therefore decreasing the number of X-rays generated. This is otherwise known as the Mass Effect (see description in Goldstein et al. 1992).

The Mass Effect follows a negative exponential relationship with increasing tilt angle, while the Absorption Effect follows a positive exponential relationship (see description in Goldstein et al. 1992). The result is that with initial tilts, the Absorption Effect dominates and therefore the X-ray counts increase as more are able to escape. At higher angles, the Mass Effect takes over as the X-ray generation volume decrease dominates and X-ray counts decrease. This is illustrated in Fig. 10, and accounts for the initial increase and then decrease in counts seen in Fig. 7. The low Fe content of our olivine may account for less obvious nature of this trend in the Fe data.

In addition, the intensity of X-ray absorption is energy dependent, being biased towards absorption of lower energy X-rays. As the sample is tilted, and absorption decreases, the lower energy X-rays therefore increase at a higher rate than the higher energy X-rays (Curgenven and Duncumb 1971; Duncumb 1971). As Si-Kα X-rays are of a higher energy than those of Mg-Kα, this is qualitatively compatible with the increase in Mg relative to Si as exhibited in Fig. 8.

As the region of residue analysis is restricted to a small crescent shape within the crater by geometry (Imaging and Analysis Method section), we can be confident that for craters
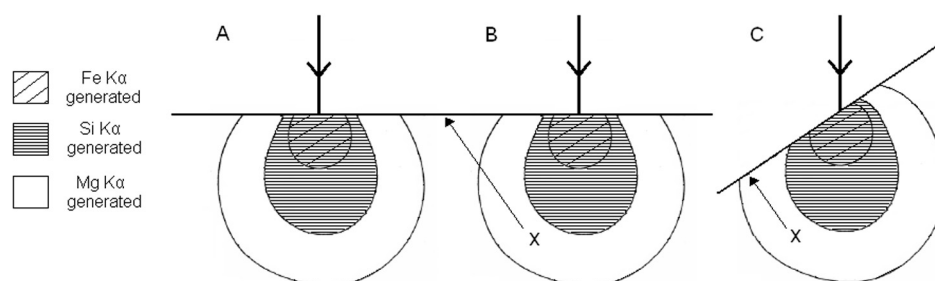
Fig. 9. Illustrating the effect of sample tilt on X-ray counts (Note: not to scale). A) The X-ray generation volumes for different energy X-rays—the beam energy decreases with depth due to elastic scattering. B) 0° sample tilt; the X-ray generation volume is a maximum and the path length to the surface (path indicated by an arrow) for an X-ray generated at "x" is large, meaning a higher probability of being absorbed. C) As the sample is tilted the X-ray generation volume decreases but so does the path length. For low tilt angles the decrease in path length will be more dramatic than the decrease in X-ray generation volume, but as higher tilt angles are employed, the decrease in X-ray generation volume will become the controlling factor.

of this dimension our residue analyses have been taken from highly tilted areas resulting in high beam incidence angles (greater than ~60°). Given that our projectile analyses were all taken with incidence angles of ~0°, while those for our residue analyses fall within this range of 60 to 80°, the angle of beam incidence could potentially account for at least ½ of our ~10% olivine projectile-to-residue Mg to Si compositional discrepancy.

Influence of Sample Morphology: Homogenous Projectiles versus Thin Layers of Residue

Differences in the morphology of residues and projectiles may also contribute to the observed changes in Mg to Si ratio. The thinness of the crater residues results in a significant proportion of the X-ray generating volume being located within the aluminum substrate (shown by the high Al counts). As a result, while Fig. 9 may adequately illustrate the beam interaction and primary beam-stimulated Mg and Si X-ray generation volumes during analysis of projectile material, it is not appropriate for many thin residues. Here, the Mg and Si primary X-ray generation volumes cut-off at the lower limit of the residue layer, and if this is shallower than the 'escape depth' (the limit from which X-rays are able to escape rather than be absorbed), counts for these elements will be lower than might otherwise be expected. As the Mg X-ray generation volume extends to a greater depth than the Si (although the Mg escape depth is concomitantly shallower), we might expect any cut-off to have a more significant effect on the Mg counts. Therefore, when comparing projectile against residue data, we might expect a decrease in the Mg to Si ratio.

An additional complication to our data brought about by the different sample morphologies concerns the phenomenon of secondary fluorescence (SF): X-rays generated by one element stimulating the production of lower energy X-rays in another element (see description in Goldstein et al. 1992). Standard matrix correction routines can be applied to account for this effect in flat, homogenous samples like the projectiles. However, as the geometry of crater topography prohibits
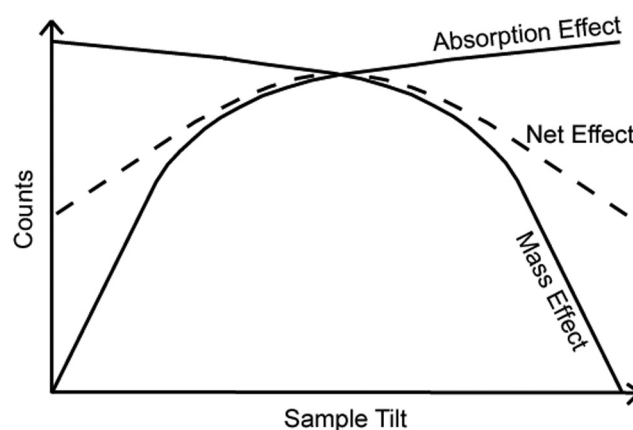

Fig. 10. Schematic diagram illustrating the style (not to scale) of the net effect (dashed line) of absorption and mass effects (solid lines) on X-ray counts. X-ray absorption is linearly dependent upon the path length within the sample, and thus is a function of the inverse sine of the take-off angle. Inversely, X-ray escape, is proportional to the sine of the tilt angle. The net effect is to initially increase X-ray counts as the decrease in absorption dominates, then decrease X-ray counts as the mass effect dominates.

reliable matrix modelling, we cannot make quantitative correction for SF during our comparisons, which may accentuate apparent differences between the projectile and residue raw X-ray count data. Nevertheless, we can consider the likely degree of influence. In the analyses of projectiles, Mg and Si X-rays were generated in a roughly hemispherical volume below the surface (as in Fig. 9A), entirely within the silicate projectile material. Some of the generated Si-Kα X-rays (~1.74 keV) are absorbed along their path length, producing Mg-Kα X-rays (~1.25 keV). Si-Kα X-rays have a higher probability of being absorbed and inducing SF if generated at greater depth. In contrast, for the residue analyses, Si-Kα X-rays can only be generated in the thin surface layer, and so have short path lengths, and consequently a higher probability of escape rather than absorption and generation of Mg-SF. The lack of deeper-generated Si-Kα X-rays, therefore might give an apparent
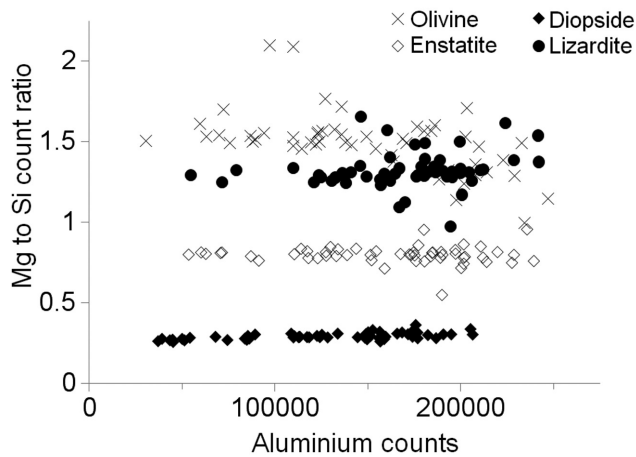
Fig. 11. Mg to Si count integral ratios plotted against raw Al count integrals in EDX spectra taken from the initial magnesium silicate impact residues.

decrease in the ratio of Mg to Si for the residue analyses, as the Mg counts no longer include a contribution by SF induced by Si.

However, while Si-induced Mg-SF is decreased in residue analyses, the presence of the Al foil beneath and around residues provides an important alternative source of X-rays. The energies of the Al-Kα X-rays generated by the electron beam penetrating through the residue into the Al substrate lie above those of Mg and below Si. They can generate SF of Mg-, but not Si-Kα, thereby increasing detection of Mg- relative to Si-Kα from the residues. SF is known to be more efficient when the energies of the primary and secondary X-ray are similar (see description in Goldstein et al. 1992). The smaller difference in energy between Al- and Mg-Kα X-rays compared to Si- and Mg-Kα X-rays therefore means that the Al-Kα X-rays are more efficiently absorbed and more successful at inducing SF in the Mg. As a result, the SF induced by the Al substrate beneath a thin layer of residue is likely to be greater than would have been induced by Si in the homogenous projectile, and therefore the Mg to Si ratio will appear to have increased in the residue. However, the low energy tail of a very large Al Kα peak may also raise the local Brehmstrahlung causing problems for accurate background fitting beneath the Mg-Kα peak, and an apparent decrease in Mg counts. This effect will probably be most marked in the thinnest residues with a major contrast between size of Mg Kα and Al Kα.

The extent of the Mg- and Si-Kα X-ray generation volumes, as well as SF (by Al and Si) and Al peak interference, should be influenced by the thickness of the residue. With thinner residues the Si-Kα X-rays generated will have shorter path lengths making them even less likely to induce Mg-SF. Additional complications arise as the beam will penetrate deeper into the Al substrate, generating more Al-Kα X-rays which are capable of causing Mg-SF but also an increase in the background beneath the Mg peak. However,

a thinner residue also means lower Mg and Si counts at the outset and less material in which to cause Mg-SF. If any of these factors makes a significant contribution to the detected X-ray signal, variation in thickness should ultimately cause scatter of the residue data for any analyzed mineral residue.

This combination of morphological effects gives an extremely complicated situation, with many unconstrained variables. Unlike our beam incidence investigation (Angle of Beam-Sample Incidence section), we can present no simple experiment that can quantify the overall effect of the differing morphologies, especially as residues may be very irregular in thickness and orientation, and can even be intimately interlayered (Kearsley et al. 2007). Nor can we predict from theory alone whether the effects described above should result in a systematic increase or decrease in the Mg to Si ratio between residue and projectile. Nevertheless, our data show that there really is such an increase in apparent Mg to Si ratio from projectile materials to their residues in craters.

Fortunately, we can determine whether a correlation exists between the Mg to Si count ratio of residues and their "thickness." For every spectrum we obtained, the Mg to Si count ratio was plotted against Al counts, a proxy for residue thickness (as we might assume that residue thickness should have a direct effect on the number of Al-Kα X-rays recorded, with thinner residues allowing increased beam penetration into the Al substrate and therefore higher Al counts). From these data plots (Fig. 11), trend lines were fitted and their equations established. The data for olivine, enstatite and lizardite residues showed broad scatter, especially towards larger Al count values, accompanied by low count totals for Mg and Si. Unfortunately, in most EDX detectors (including that used in this study), the lower X-ray detection efficiency and complex Bremsstrahlung shape seen in the spectrum below 2 keV make background fitting difficult for closely spaced peaks such as Mg- and Al-Kα. Not only does the low energy tail of the large Al peak overlap Mg (as described above), resulting in poorer background definition and hence worse peak area recognition, but the Bremsstrahlung shape is also highly dependent on local micrometer-scale topography. This can also produce much greater dispersion of apparent Mg count rates, especially decreased apparent Mg relative to Si. Given this demonstrably poor precision, we used the convention that the gradient of our trend lines should be considered indistinguishable from a zero value (i.e., Mg to Si count ratio is effectively constant with increased Al counts) if the numerical fit error was >3 times the value of the slope. For diopside and olivine, with slopes 5 and 4 times greater than error respectively, there appears to be a real change in Mg to Si count ratio with Al counts (thickness). However, exclusion of those data points with low Mg and Si totals (Mg + Si < 5% of the total Al-Kα X-rays counted) produces olivine, enstatite and lizardite trends that are compatible with a zero value gradient. Only diopside retains a systematically increasing trend in Mg to Si count ratio that could be attributable to a

wide range of residue thickness. It therefore appears that for at least the olivine, enstatite and lizardite, the determined Mg to Si count ratio is relatively insensitive to residue thickness effects, provided that the thickness is great enough to generate a sufficient number of these X-rays so as to avoid poor background definition as described above. Conversely, this highlights the limitations of reliable in situ mineral identification by count-rate ratios for very thin residues such as those found in smaller craters (<20 μm diameter).

Loss of Silicon

Bernard and Hörz (1995) suggested that at high speed (i.e., the velocity of the Stardust impact), the majority of the projectile should experience pressures high enough to melt it, and indeed some parts may reach pressures high enough to cause vaporization. Burchell and Kearsley (2008) estimated that at 6 km s^{-1}, minerals are shocked to peak pressures of 60 to 90 GPa during impacts on aluminum. Vaporized material may easily be lost permanently from the crater area, and we might therefore expect loss to be biased towards the more volatile elements. Work by Kearsley et al. (2007b) and Wozniakiewicz et al. (2007, 2008) on sulfide residues clearly shows the more volatile S is lost relative to Fe during impact. Although the elemental boiling points of Mg and Si (1090 °C and 2355 °C, respectively [see Lide 2009]) might suggest that such loss should be biased towards Mg, the volatility of an element is likely controlled by its bonding in the host material. Therefore we would be unwise to use elemental boiling points for a comparison of volatility in silicates. The work of Lodders (2001) describes Si and Mg as being of similar volatility based on their condensation temperatures when forming forsterite, although it must be borne in mind that this refers to their condensation temperatures and not their vaporization temperatures. A more relevant comparison of volatility may be found in the work of Hashimoto (1983). In those experiments, data obtained during the evaporation of a multicomponent melt revealed the higher volatility of SiO_2 compared to MgO. Our increased Mg to Si ratio may therefore be the result of the loss of more volatile Si in these silicates. Gerasimov et al. (2000) have also described the selective volatilization of elements in laser heating experiments vaporizing various silicates, including augite, although the peak temperature may be very high (estimated to be 4000 to 5000 K) and sustained for a relatively long period (~10^{-3} s). In their results it was apparent that during the heating event, while Si exhibited progressive depletion in impact melts as mass loss increased, Mg initially remained in the melt, resulting in enrichment relative to Si. As heating continued the Mg too was lost. For our impacts, however, the heating is almost instantaneous (on the order of ~10^{-9} s assuming the duration of the contact and compression stage is roughly equal to the time taken for the projectile to traverse its own diameter, i.e., the impactor diameter divided by the impact velocity [see Melosh 1989]), with heat being quickly

conducted away by the metal target. It could, therefore, be possible that the second stage (loss of Mg) does not occur, resulting in enrichment of Mg relative to Si. If Si is preferentially lost, then it could further be inferred that the degree of Si loss (and maintenance of Mg) is dependent on the structure of the host mineral.

Intriguingly the cratering PE sub-team reported the occurrence of stoichiometric magnesium silicate compositions in some residues (Hörz et al. 2006). If Si is preferentially lost, this would not be possible. Looking at their analytical technique, we find that their analyses were conducted with the foils tilted to "reach" the residue, thereby also enabling perpendicular beam incidence (as illustrated in Kearsley et al. 2007b). These seemingly conflicting results may be resolved by considering the distribution of different impact residue components. Bernard and Hörz (1995) report that if solid crystalline (stoichiometric) mineral fragments remain they are more likely to be located in the central region of the pit where PE analyses were taken, while the melt—which is more likely to have suffered loss of Si—creeps up the sides of the crater where (typically) our analyses were taken.

Plots of only the two elements, Mg and Si, are an effective way of delineating and comparing these four magnesium silicates. However, if additional magnesium silicates and indeed olivines of different compositions are to be included, it is clear that the diagrams would become cluttered and mineral assignments ambiguous. Therefore in the next section where we address the olivine suite, ternary diagrams have been constructed to include Mg-Kα, Si-Kα and Fe-Kα count comparisons. Finally, to complete the investigation, ternary diagrams have also been constructed for the initial magnesium silicates.

Olivines

For the suite of olivines, a ternary diagram was generated for each composition to include the Fe counts (Fig. 12). Plotted on each ternary diagram are Mg, Fe and Si counts for the original projectiles and the resulting residues. As discussed in the Impurities in the Projectiles section, the olivines used here are often composed of a mixture of precursor minerals, intermediate melt, and resulting olivine, therefore the individual projectile components have been plotted separately on these diagrams. Taking this approach, the olivine components for each composition sit as well defined, separate groups for every mineral except Fo_{60}—the spread seen for Fo_{60} mimics the varied composition witnessed in this sample when examined in the Impurities in the Projectiles section.

Lines marking constant Mg to Si counts, Si to Fe counts and Mg to Fe counts based on the average (olivine component of the) projectile composition, have been added to Fig. 12 to make it clear how the materials have changed during impact
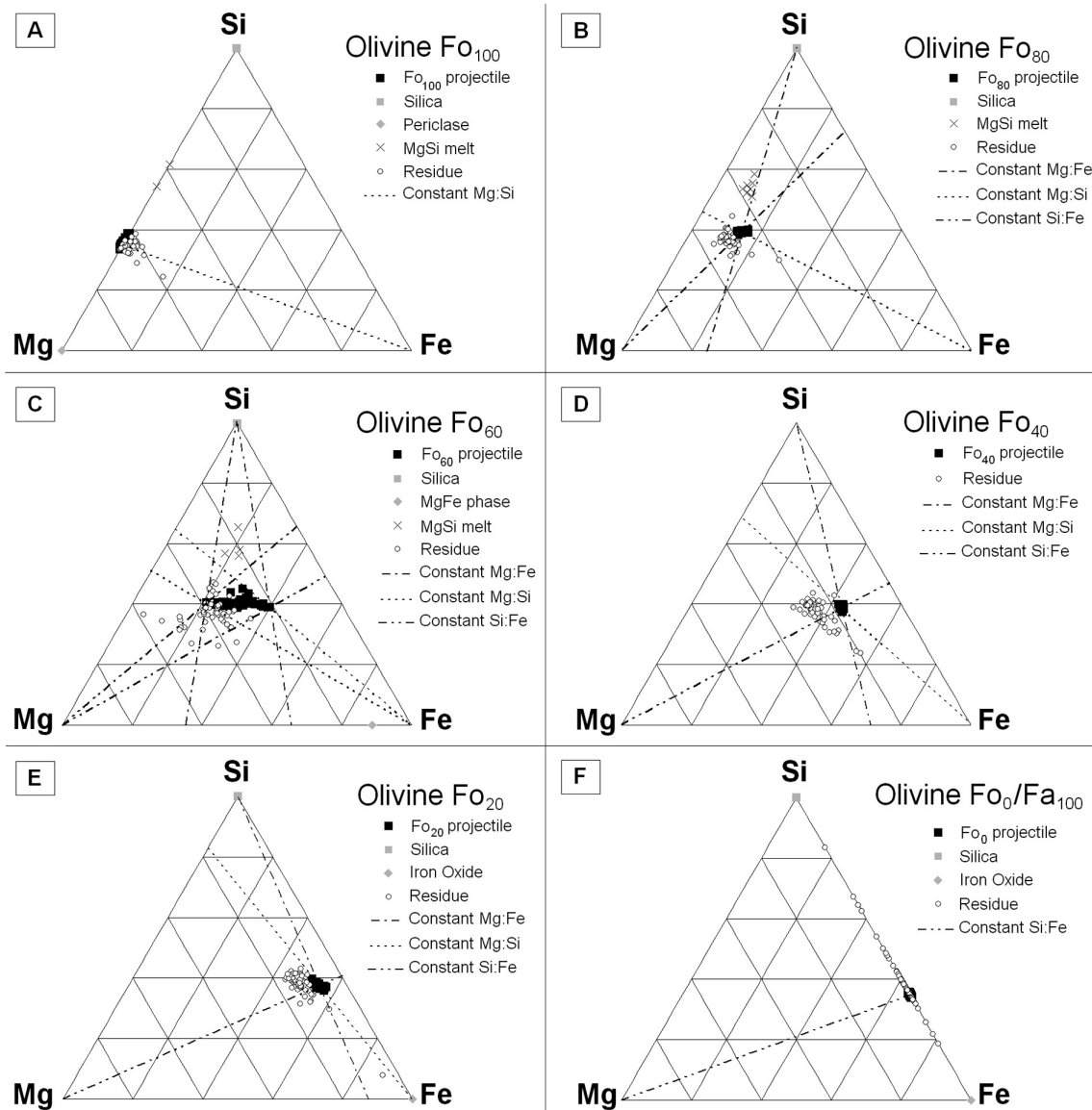
Fig. 12. Ternary diagrams for the olivine suite displaying relative Mg, Si and Fe X-ray count integrals from EDX analyses of polished projectiles (both the intended olivine grains and the associated impurities) compared to rough residues on crater walls. Lines of constant Mg: Si, Si:Fe and Mg:Fe are shown to delineate specific changes between projectile and residue. There is a general increase in Mg relative to Si and also to Fe for residue data compared to projectile data. Note the deviations from this trend can be explained by mixing with impurities in the projectile as well as foil inclusions.

(for Fo_{60} two versions of each of these lines have been added according to the end members of its compositional range rather than average projectile composition). When residue results are plotted we see indications of a general increase in Mg relative to both Si and Fe for Fo_{20}, Fo_{40}, Fo_{60} and Fo_{80} (Fo_0 has no Mg in the first place and Fo_{100} cannot increase in Mg). This has subsequently been confirmed and revealed as a systematic increase, like that for the initial magnesium silicates Mg and Si plots, by plotting Mg against Si and then Mg against Fe as separate two component graphs. An increase in the Mg to Si ratio was exhibited by our initial magnesium silicates and as such the explanations of the Magnesium

Silicates section still stand. These can also be applied successfully to the change in Mg to Fe ratio; plotting the sample tilt against the Mg to Fe count ratio we see a similar increase in Mg relative to Fe with increased sample tilt, the Fe-Kα line lies far above that of Al therefore will not experience secondary fluorescence or peak interference, and Fe also exhibits initial preferential loss compared to Mg when evaporating (Hashimoto 1983; Gerasimov et al. 2000). An increase in Mg relative to Fe and Si can therefore be put down to analysis procedure and possibly some preferential loss of Fe and Si relative to Mg. Correction for matrix effects on the apparent Mg to Fe ratio due to variable beam-sample
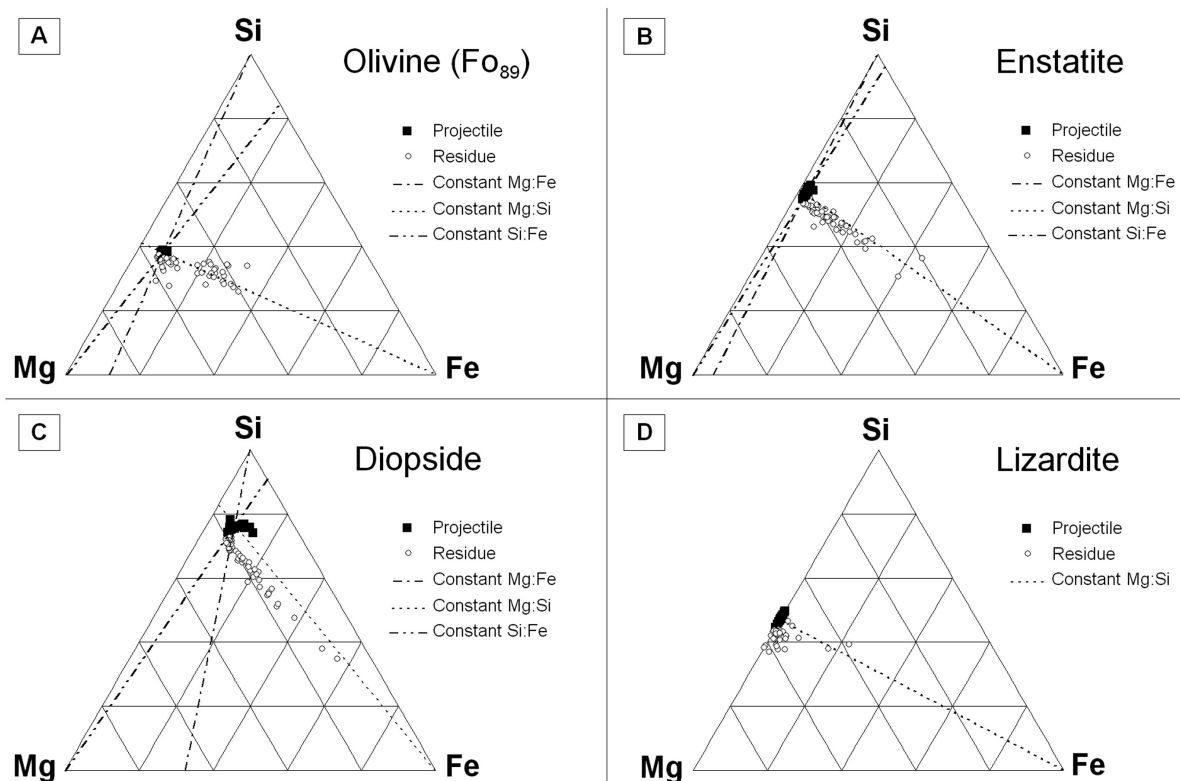
Fig. 13. Ternary diagrams for initial magnesium silicates displaying raw relative Mg, Si and Fe X-ray count integrals from EDX analyses of near horizontal areas of projectile grains compared to rough residues on crater walls. Lines of constant Mg:Si, Si:Fe and Mg:Fe are shown to delineate specific changes between projectile and residue. Note the varied increase in Fe relative to Mg for the residue compared to projectiles.

geometry could in theory be further improved by using Fe-Lα (whose energy and therefore interaction volume are much closer to Mg-Kα). However, for at least the initial suite of magnesium silicates studied, the very low Fe content and low detector efficiency at such low energy meant that this suite of Fe peaks were small and significantly overlapped by the O-Kα peak. The complex Bremsstrahlung shape (locally modified by topography) also made background fitting and peak area measurement unreliable. Given these problems, and in order to keep analyses consistent from one mineral to the next, Fe-Kα data was used throughout the investigation.

While this increase in Mg relative to Si and Fe is the general trend, some data plot towards an enrichment in Si or Fe. In these cases it is likely that mixing of the olivine with other projectile components has occurred during the impact (as highlighted in the Impurities in the Projectiles section). Increases in Fe and Si content could also be the result of the analyses being taken over an area containing Fe or Si rich inclusions as described in the Impurities in the Target section.

Indeed, plotting the ternary diagrams for the initial magnesium silicates (Fig. 13) also highlights the significant problems posed by the foil inclusions. Unlike the suite of olivines, the initial magnesium silicates display a general increase in Fe relative to Mg. Plotting Mg against Fe alone makes it apparent that, in contrast to the systematic change for the olivine suite, the degree of increase in Fe here is

highly variable. This is illustrated in Fig. 14, where Mg counts have been plotted against Fe counts for Fo$_{80}$ (olivine suite) and the initial magnesium silicate olivine (Fo$_{89}$). The Fo$_{80}$ residue displays little spread but a clear increase in Mg relative to Fe compared to the data of the original projectile, while Fo$_{89}$ has a more ambiguous trend generally indicating an increase in Fe relative to Mg when compared to the data of the original projectile. As both analysis technique and impact loss have been shown to raise Mg counts relative to both Si and Fe, this varied increase in Fe must be caused by some introduction of Fe to the sample, most likely from the foil inclusions. The three initial magnesium silicates—olivine (Fo$_{89}$), enstatite, and diopside—all impacted the same foil, therefore taking into account the random spread of inclusions, this increase in Fe in all three suggests that this section of foil may well have been host to a cluster of inclusions. It is clear that the iron inclusions could pose a significant obstacle to interpretation of these and possibly other forms of residue analyses. Just how much of an obstacle would require further, higher resolution investigation into the exact nature of the interaction between projectile and target upon impact, a topic for later work.

For this investigation, using SEM-EDX we have, however, shown that after impact these mineral residues have remained distinct from one another (Fig. 15). Although residue chemical analyses appear modified from
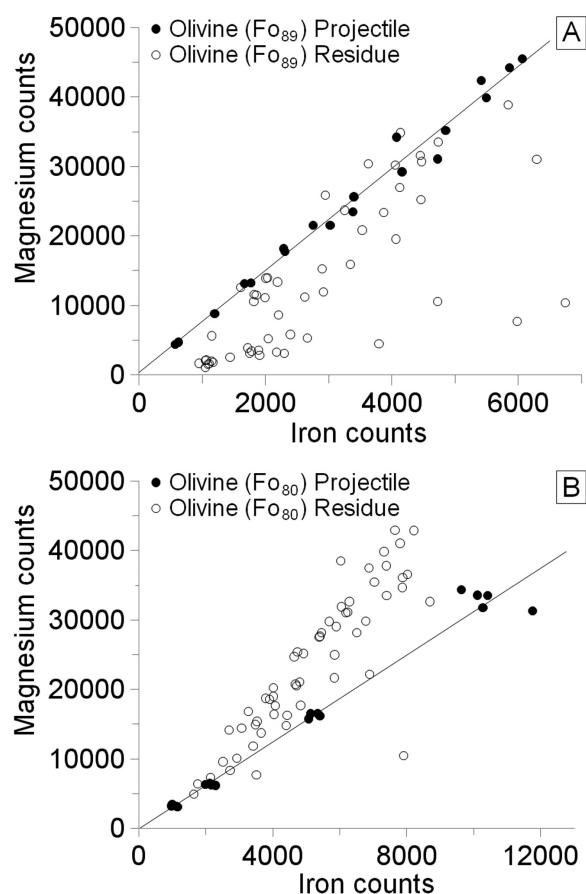
Fig. 14. Raw Mg and Fe count integrals in EDX spectra taken from projectile and residue of A) the initial olivine (Fo_{89}) and B) the olivine suite Fo_{80}. Solid lines represent the linear fits to the projectile data.
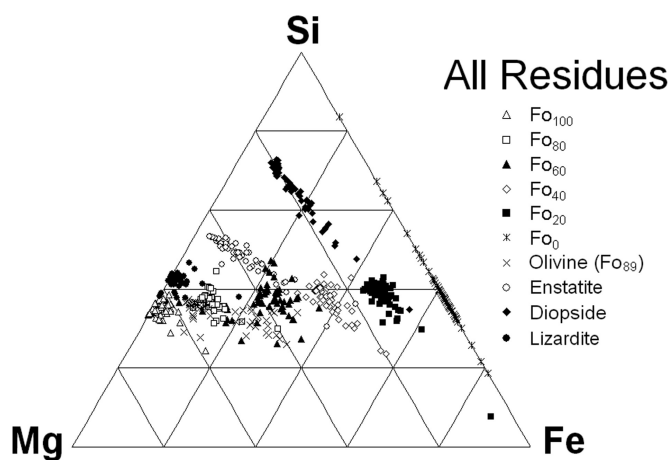

Fig. 15. Ternary diagram displaying relative Mg, Si and Fe X-ray count integrals from EDX analyses of all residues analyzed in this work. Residues remain distinct despite complicated composition of initial projectiles.

their projectiles, the process appears to be relatively predictable, raising the possibility that we can calibrate the effect on individual grains in the Stardust materials. The

extent to which a definite compositional precursor for Stardust residues can be deduced from such analyses, however, is dependent upon on the nature and extent of modification experienced by these impactors—while compositions of single component homogenous impacting particles may be easily deduced, impact heating may lead to melting and mixing of chemistries in a multi-component impactor. The nature and extent of alteration experienced by different minerals will therefore be the focus of future investigations.

CONCLUSION

Members of both the initial magnesium silicates and the suite of synthetic olivines investigated in this paper have remained distinct from one another after the impact process (at 6 km s^{-1} into aluminium foil), although an increase in their Mg counts relative to Si is consistently observed in all cases in SEM-EDX analysis. The olivine suite of projectiles also exhibited a general increase in Mg relative to Fe counts. Biasing of the Mg counts relative to Si and Fe in the residues appears largely due to the analysis procedure however, there remains the possibility that we have real preferential loss of Si and Fe relative to Mg during impact.

This investigation into preferential loss of elements during impact only addresses three key elements. However, it does highlight the importance of research into the effects of capture heating on different impacting materials. If, as seems likely, grains impacted onto Stardust foils experienced similar changes in chemistry it is very important that we determine the nature of these changes before interpreting analytical results and drawing conclusions as to the original chemistry of the cometary grains. It is also important to determine the linkage between change in composition and structural/ mineralogical modification of the impactor. In further work it is our ambition to constrain the effect of capture heating on the complete suite of Stardust materials (silicates, sulfides, metals, etc.) and investigate potential controlling factors such as style of structural preservation. This may potentially allow us to re-calculate primary composition from residue composition.

The work of this paper has also drawn attention to the possible complications to interpretation brought about by foil inclusions and multi-component projectiles. While an apparent increase in Mg relative to Si and Fe is the general trend identified for these mineral residues, some residue data points are enriched in Si and/or Fe relative to their initial projectile compositions. In projectiles where there is evidence of multi-component regions, the mixture during impact can cause apparent increase in Si and Fe. Presently, a number of Stardust impactors have been identified as multi-component particles (Hörz et al. 2006; Zolensky et al. 2006; Kearsley et al. 2008). If mixing does occur between separate components, interpretation and identification of residues of such grains will be complicated. In the foil, an increase in Fe

and Si counts may also result from impact over the site of Fe- or Si-rich alloy inclusions. It is these inclusions that are believed to be behind the results of the initial magnesium silicates where, unlike the olivine suite, a varied increase in Fe relative to Mg is observed. Hence, interference from the foil inclusions and residue component mixing may both obscure the real stoichiometric relationships.

It is clear that, while precise compositional identification may not as yet be possible for all impact residues in all cases by this method, the main groups of mafic silicates can be easily and reliably distinguished in EDX analyses performed in rapid surveys of Stardust foil craters, enabling access to a valuable additional collection of cometary materials.

Editorial Handling—Dr. Donald Brownlee

REFERENCES

Bernhard R. P. and Hörz F. 1995. Craters in aluminium 1100 by soda-lime glass spheres at 1 to 7 km/s. *International Journal of Impact Engineering* 17:69–80.

Bernhard R. P., Durin C., and Zolensky M. E. 1992. Scanning electron microscope/energy dispersive X-ray analysis of impact residues in LDEF tray clamps. NASA Langley Research Center Second LDEF Post-Retrieval Symposium Abstracts. p. 45.

Bernhard R. P., See T. H., and Hörz F. 1993. Projectile compositions and modal frequencies on the "Chemistry of Micrometeoroids" LDEF experiments. NASA Langley Research Center LDEF 69 Months in Space. Second Post-Retrieval Symposium, Part 2. pp. 551–573.

Bernard R. P., Barrett R. A., and Zolensky M. E. 1995. Analytical electron microscopy of LDEF impactor residues. NASA Langley Research Center LDEF 69 Months in Space. Third Post-Retrieval Symposium, Part 1. pp. 401–413.

Bland P. A., Cressey G., and Menzies O. N. 2004. Modal mineralogy of carbonaceous chondrites by X-ray diffraction and Mössbauer spectroscopy. *Meteoritics & Planetary Science* 39:3–16.

Brownlee D. E., Tsou P., Anderson J. D., Hanner M. S., Newburn R. L., Sekanina Z., Clark B. C., Hörz F., Zolensky M. E., Kissel J., McDonnell J. A. M., Sandford S. A., and Tuzzolino A. J. 2003. Stardust: Comet and interstellar dust sample return mission. *Journal of Geophysical Research (Planets)* 108(E10):8111.

Brownlee D. E., Tsou P., Aléon J., Alexander C. M. O'D., Araki T., Bajt S., Baratta G. A., Bastien R., Bland P. A., Bleuet P., Borg J., Bradley J. P., Brearley A., Brenker F., Brennan S., Bridges. J. C., Browning N. D., Brucato J. R., Bullock E., Burchell M. J., Busemann H., Butterworth A., Chaussidon M., Cheuvront A., Chi M., Cintala M. J., Clark B. C., Clemett S. J., Cody G., Colangeli L., Cooper G., Cordier P., Daghlian C., Dai Z. R., D'Hendecourt L., Djouadi Z., Dominguez G., Duxbury T., Dworkin J. P., Ebel D. S., Economou T. E., Fakra S., Fairey S. A.

J., Fallon S., Ferrini G., Ferroir T., Fleckenstein H., Floss C., Flynn G., Franchi I. A., Fries M., Gainsforth Z., Gallien J. -P., Genge M., Gilles M. K., Gillet P., Gilmour J., Glavin D. P., Gounelle M., Grady M. M., Graham G. A., Grant P. G., Green S. F., Grossemy F., Grossman J. N., Guan Y., Hagiya K., Harvey R., Heck P., Herzog G. F., Hoppe P., Hörz F., Huth J., Hutcheon I. D., Ignatyev K., Ishii H., Ito M., Jacob D., Jacobsen S., Jones S., Joswiak D., Jurewicz A., Kearsley A. T., Keller L. P., Khodja H., Kilcoyne A. L. D., Kissel J., Krot A., Langenhorst F., Lanzirotti A., Le L., Leshin L. A., Leitner J., Lemelle L., Leroux H., Liu M.-C., Luening K., Lyon I., MacPherson G., Marcus M. A., Marhas K., Marty B., Matrajt G., McKeegan K., Meibom A., Mennella V., Messenger K., Messenger S., Mikouchi T., Mostefaoui S., Nakamura T., Nakano T., Newville M., Nittler L. R., Ohnishi I., Ohsumi K., Okudaira K., Papanastassiou D. A., Palma R., Palumbo M. E., Pepin R. O., Perkins D., Perronnet M., Pianetta P., Rao W., Rietmeijer F. J. M., Robert F., Rost D., Rotundi A., Ryan R., Sandford S. A., Schwandt C. S., See T. H., Schlutter D., Sheffield-Parker J., Simionovici A., Simon S., Sitnitsky I., Snead C. J., Spencer M. K., Stadermann F. J., Steele A., Stephan T., Stroud R., Susini J., Sutton S. R., Suzuki Y., Taheri M., Taylor S., Teslich N., Tomeoka K., Tomioka N., Toppani A., Trigo-Rodríguez J. M., Troadec D., Tsuchiyama A., Tuzzolino A. J., Tyliszczak T., Uesugi K., Velbel M., Vellenga J., Vicenzi E., Vincze L., Warren J., Weber I., Weisberg M., Westphal A., Wirick S., Wooden D., Wopenka B., Wozniakiewicz P. J., Wright I., Yabuta H., Yano H., Young E. D., Zare R. N., Zega T., Ziegler K., Zimmermann L., Zinner E., and Zolensky M. 2006. Comet 8P/Wild 2 under a microscope. *Science* 314:1711–1716.

Burchell M. J., Cole M. J., McDonnell J. A. M., and Zarnecki J. C. 1999. Hypervelocity impact studies using the 2 MV Van de Graaff dust accelerator and two stage Light Gas Gun of the University of Kent at Canterbury. *Measurement Science and Technology* 10:41–50.

Burchell M. J., Fairey S. A. J., Wozniakiewicz P., Brownlee D. E., Hörz F., Kearsley A. T., See T. H., Westphal A., Green S. F., Trigo-Rodríguez J. M. 2008a. Characteristics of cometary dust tracks in Stardust aerogel and laboratory calibrations. *Meteoritics & Planetary Science* 43:23–40.

Burchell M. J., Foster N. J., Kearsley A. T., and Creighton J. A. 2008b. Identification of mineral impactors in hypervelocity impact craters in aluminum by Raman spectroscopy of residues. *Meteoritics & Planetary Science* 43:135–143.

Burchell M. J., and Kearsley A. T. 2008. Short period Jupiter-family comets after Stardust. *Planetary and Space Science* 57(10):1146–1161.

Campins H. and Swindle T. D. 1998. Expected characteristics of cometary meteorites. *Meteoritics & Planetary Science* 33:1201–1211.

Curgenven L., and Duncomb P. 1971. Tube Investments Research Laboratories Report 303.

Davis J. R. 1998. *Metals handbook*. Desk edition. 2nd ed. Materials Park, Ohio, USA: ASM International.

Duncomb P. 1971. Proceedings, Electron Microscopy and Analysis Group. Institute of Physics, London, Conference Series, vol. 10. p. 132.

Flynn G. J., Bleuet P., Borg J., Bradley J. P., Brenker F. E., Brennan S., Bridges J., Brownlee D. E., Bullock E. S., Burghammer M., Clark B. C., Dai Z. R., Dahlian C. P., Djouadi Z., Fakra S., Ferroir T., Floss C., Franchi I. A., Gainsforth Z., Gallien J.-P., Gillet P., Grant P. G., Graham G. A., Green S. F., Grossemy F., Heck P. R., Herzog G. F., Hoppe P., Hörz F., Huth J., Ignatyev K., Ishii H., Janssens K., Joswiak D., Kearsley A. T., Khodja H., Lanzirotti A., Leitner J., Lemelle L., Leroux H., Luening K., MacPherson

G., Marhas K. K., Marcus M. A., Matrajt G., Nakamura T., Nakamura-Messenger K., Nakano T., Newville M., Papanastassiou D. A., Pianetta P., Rao W., Riekel C., Rietmeijer F. J. M., Rost D., Schwandt C. S., See T. H., Sheffield-Parker J., Simionovici A., Sitnitsky I., Snead C. J., Stadermann F. J., Stephan T., Stroud R. M., Susini J., Suzuki Y., Sutton S. R., Taylor S., Teslich N., Troadec D., Tsou P., Tsuchiyama A., Uesugi K., Vekemans B., Vicenzi E. P., Vincze L., Westphal A. J., Wozniakiewicz P. J., Zinner E., and Zolensky M. E. 2006. Elemental compositions of comet 81P/Wild 2 collected by Stardust. *Science* 314:1731–1735.

Foster N. J., Wozniakiewicz P. J., Burchell M. J., Kearsley A. T., Creighton A. J., and Cole M. J. 2007. Identification by Raman spectroscopy of processing effects in forsterite-fayalite samples during hypervelocity impacts on foils and capture in aerogel (abstract #5186). *Meteoritics & Planetary Sciences* 42:A51.

Goldstein J. I., Newbury D. E., Echlin P., Joy C. D., Romig A. D. Jr., Lyman C. E., Fiori C., and Lifshin E. 1992. *Scanning electron microscopy and X-ray microanalysis*, 2nd ed. New York-London: Plenum Press.

Graham G. A., Sexton A., Grady M. M., and Wright I. P. 1997. Further attempts to constrain the nature of the impact residues in the HST solar array panels. *Advances in Space Research* 20: 1461–1465.

Graham G. A., Kearsley A. T., Grady M. M., Wright I. P., Griffiths A. D., and McDonnell J. A. M. 1999. Hypervelocity impacts in low Earth orbit: Cosmic dust versus space debris. *Advances in Space Research* 23:95–100.

Graham G. A., Kearsley A. T., Drolshagen G., McBride N., Green S. F., and Wright I. P. 2001a. Microparticle impacts upon HST solar cells. *Advances in Space Research* 28:1341–1346.

Graham G. A., Kearsley A. T., Wright I. P., Grady M. M., Drolshagen G., McBride N. M., Green S. F., Burchell M. J., Yano H., and Elliott R. 2001b. Analysis of impact residues on spacecraft surfaces: Possibilities and problems. In *Proceedings of the Third European Conference on Space Debris*. ESA Special Publication 473. pp. 197–203.

Gerasimov M. V., Dikov Yu. P., Yakovlev O. I., and Wlotzka F. 2000. Evaporative differentiation of impact-produced melts: Laser-simulation experiments and comparison with impact glasses from the Logoisk crater. In *Large meteorite impacts III*, edited by Kenkmann T., Hörz F., and Deutsch A. The Geological Society of America Special Paper 384. pp. 351–366.

Hanner M. S. 2003. The Mineralogy of cometary dust. In *Astromineralogy*, edited by Henning T. K. Berlin: Springer-Verlag. pp. 171–188.

Hashimoto A. 1983. Evaporation metamorphism in the early solar nebula—Evaporation experiments on the melt $FeO-MgO-SiO_2-CaO-Al_2O_3$ and chemical fractionations of primitive materials. *Geochemical Journal* 17:111–145.

Hörz F., Bastien R., Borg J., Bradley J. P., Bridges J. C., Brownlee D. E., Burchell M. J., Chi M., Cintala M. J., Dai Z. R., Djouadi Z., Dominguez G., Economou T. E., Fairey S. A. J., Floss C., Franchi I. A., Graham G. A, Green S. F., Heck P., Hoppe P., Huth J., Ishii H., Kearsley A. T., Kissel J., Leitner J., Leroux H., Marhas K., Messenger K., Schwandt C. S., See T. S., Snead C., Stadermann F. J., Stephan T., Stroud R., Teslich N., Trigo-Rodríguez J. M., Tuzzolino A. J., Troadec D., Tsou P., Warren J., Westphal A., Wozniakiewicz P. J., Wright I., and Zinner E. 2006. Impact features on Stardust: Implications for comet 81P/Wild 2 dust. *Science* 314:1716–1719.

Kearsley A. T., Drolshagen G., McDonnell J. A. M., Mandeville J.-C., and Moussi A. 2005. Impacts on Hubble Space Telescope solar arrays: Discrimination between the natural and man-made particles. *Advances in Space Research* 35:1254–1262.

Kearsley A. T., Burchell M. J., Hörz F., Cole M. J., and Schwandt C. S., 2006. Laboratory simulation of impacts on aluminium foils of the Stardust spacecraft: Calibration of dust particle size from comet Wild 2. *Meteoritics & Planetary Science* 41:167–180.

Kearsley A. T., Graham G. A., McDonnell J. A. M., Taylor E. A., Drolshagen G., Chater R. J., McPhail D., and Burchell M. J. 2007a. The chemical composition of micrometeoroids impacting upon the solar arrays of the Hubble Space Telescope. *Advances in Space Research* 39:590–604.

Kearsley A. T., Graham G. A., Burchell M. J., Cole M. J., Dai Z. R., Teslich N., Bradley J. P., Chater R., Wozniakiewicz P. J., Spratt J., and Jones. G. 2007b. Analytical scanning and transmission electron microscopy of laboratory impacts on Stardust aluminium foils: Interpreting impact crater morphology and the composition of impact residues. *Meteoritics & Planetary Science* 42:191–210.

Kearsley A. T. Borg J., Graham G. A., Burchell M. J., Cole M. J., Leroux H., Bridges J. C., Hörz F., Wozniakiewicz P. J., Bland P. A., Bradley J. P., Dai Z. R., Teslich N., See T., Hoppe P., Heck P. R., Huth J., Stadermann F. J., Floss C., Marhas K., Stephan T., and Leitner J. 2008. Dust from comet Wild 2: Interpreting particle size, shape, structure, and composition from impact features on the Stardust aluminium foils. *Meteoritics & Planetary Science* 43:41–74.

Leroux H., Stroud R. M., Dai Z. R., Graham G. A., Troadec D., Bradley J. P., Teslich N., Borg J., Kearsley A. T., and Hörz F. 2008. Transmission electron microscopy of cometary residues from micron-sized craters in the Stardust Al foils. *Meteoritics & Planetary Science* 43:143–160.

Lide D. R., ed. 2009. The Elements. In *CRC handbook of chemistry and physics*, 89th ed. (Internet version 2009). www.hbcpnetbase.com.

Lisse C. M., VanCleve J., Adams A. C., A'Hearn M. F., Fernández Y. R., Farnham T. L., Armus L., Grillmair C. J., Ingalls J., Belton M. J. S., Groussin O., McFadden L. A., Meech K. J., Schultz P. H., Clark B. C., Feaga L. M., and Sunshine J. M. 2006. Spitzer spectral observations of the Deep Impact ejecta. *Science* 313: 635–640.

Lodders K. 2001. Solar system abundances and condensation temperatures of the elements. *The Astrophysical Journal* 591: 1220–1247.

Melosh H. J. 1989. *Impact cratering—A geologic process*. New York: Oxford University Press. 245 p.

Menzies O. N., Bland P. A., Berry F. J., and Cressey G. 2005. A Mössbauer spectroscopy and X-ray diffraction study of the ordinary chondrites: Quantification of modal mineralogy and implications for redox conditions during metamorphism. *Meteoritics & Planetary Science* 40:1023–1042.

Rotundi A., Baratta G. A., Borg J., Brucato J. R., Busemann H., Colangeli L., D'Hendecourt L., Djouadi Z., Ferrini G., Franchi I. A., Fries M., Grossemy F., Keller L. P., Mennella V., Nakamura K., Nittler L. R., Palumbo M. E., Sandford S. A., Steele A., and Wopenka B. 2008 Combined micro-Raman, micro-infrared, and field emission scanning electron microscope analyses of comet 81P/Wild 2 particles collected by Stardust. *Meteoritics & Planetary Science* 43:367–397.

Trigo-Rodríguez J. M., Domínguez G., Burchell M. J., Hörz F., and Llorca J. 2008. Bulbous tracks arising from hypervelocity capture in aerogel. *Meteoritics & Planetary Science* 43:75–87.

Tsou P., Brownlee D. E., Sandford S. A., Hörz F., and Zolensky M. E. 2003. Wild 2 and interstellar sample collection and Earth return. *Journal of Geophysical Research (Planets)* 108(E10):8113.

Wozniakiewicz P. J., Kearsley A. T., Burchell M. J., Foster N. J., Cole M. J., Bland P. A., and Russell S. S. 2007. Analysis of residues resulting from impacts into aluminium 1145 foil: experiments to

facilitate stardust crater analyses (abstract #5199). *Meteoritics & Planetary Sciences* 42:A166.

Wozniakiewicz P. J., Kearsley A. T., Burchell M. J., Bland P. A., Ishii H. A., Dai Z. R., Teslich N., Collins G., Bradley J. P., Russell S., Cole M. J., and Lee M. 2008. Constraining the effects of capture-heating on chemistry and structure of cometary sulphides under stardust encounter conditions (abstract #1791). 39th Lunar and Planetary Science Conference. CD ROM.

Yano H., Kibe S., Deshpande S. P., and Neish M. J. 1997. The first results of meteoroid and debris analyses on the Space Flyer Unit. *Advances in Space Research* 20:1489–1494.

Yano H., Morishige K., Deshpande S. P., Maekawa Y., Kibe S., Neish M. J., and Taylor E. A. 2000. Origins of micro-craters on the SFU spacecraft derived from elemental and morphological analyses. *Advances in Space Research* 25:293–298.

Zolensky M. E., Pieters C., Clark., and Papike J. J. 2000. Small is beautiful: The analysis of nanogram-sized astromaterials. *Meteoritics & Planetary Science* 35:9–29.

Zolensky M. E., Zega T. J., Yano H., Wirick S., Westphal A. J., Weisberg M. K., Weber I., Warren J. L., Velbel M. A., Tsuchiyama A., Tsou P., Toppani A., Tomioka N., Tomeoka K., Teslich N., Taheri M., Susini J., Stroud R., Stephan T., Stadermann F. J., Snead C. J., Simon S. B., Simionovici A., See T. H., Robert F., Rietmeijer F. J. M., Rao W., Perronnet M. C., Papanastassiou D. A., Okudaira K., Ohsumi K., Ohnishi I., Nakamura-Messenger K., Nakamura T., Mostefaoui S., Mikouchi T., Meibom A., Matrajt G., Marcus M. A., Leroux H., Lemelle L., Le L., Lanzirotti A., Langenhorst F., Krot A. N., Keller L. P., Kearsley A. T., Joswiak D., Jacob D., Ishii H., Harvey R., Hagiya K., Grossman L., Grossman J. N., Graham G. A., Gounelle M., Gillet P., Genge M. J., Flynn G., Ferroir T., Fallon S., Ebel D. S., Dai Z. R., Cordier P., Clark B., Chi M., Butterworth A. L., Brownlee D. E., Bridges J. C., Brennan S., Brearley A., Bradley J. P., Bleuet P., Bland P. A., and Bastien R. 2006. Mineralogy and petrology of comet 81P/Wild 2 nucleus samples. *Science* 314:1735–1739.

Zolensky M. E., Nakamura-Messenger K., Rietmeijer F., Leroux H., Mikouchi T., Ohsumi K., Simon S., Grossman L., Stephan T., Weisberg M., Velbel M., Zega T., Stroud R., Tomeoka K., Ohnishi I., Tomioka N., Nakamura T., Matrajt G., Joswiak D., Brownlee D., Langenhorst F., Krot A., Kearsley A., Ishii H., Graham G., Dai Z. R., Chi M., Bradley J., Hagiya K., Gounelle M., and Bridges J. 2008. Comparing Wild 2 particles to chondrites and IDPs. *Meteoritics & Planetary Science* 43:261–272.